OUKA
The University of Osaka
Institutional Knowledge Archive

Title	Targeting fibroblast activation protein in solid tumors via LNP-mediated CAR-mRNA delivery promotes durable regression in murine models
Author(s)	Meng, Sikun; Hara, Tomoaki; Sato, Tetsuya et al.
Citation	Scientific Reports. 2026, 16, p. 1624
Version Type	VoR
URL	https://hdl.handle.net/11094/104040
rights	This article is licensed under a Creative Commons Attribution-NonCommercial-NoDerivatives 4.0 International License.
Note	

The University of Osaka Institutional Knowledge Archive : OUKA

https://ir.library.osaka-u.ac.jp/

The University of Osaka

scientific reports

Check for updates

OPEN

Targeting fibroblast activation protein in solid tumors via LNP-mediated CAR-mRNA delivery promotes durable regression in murine models

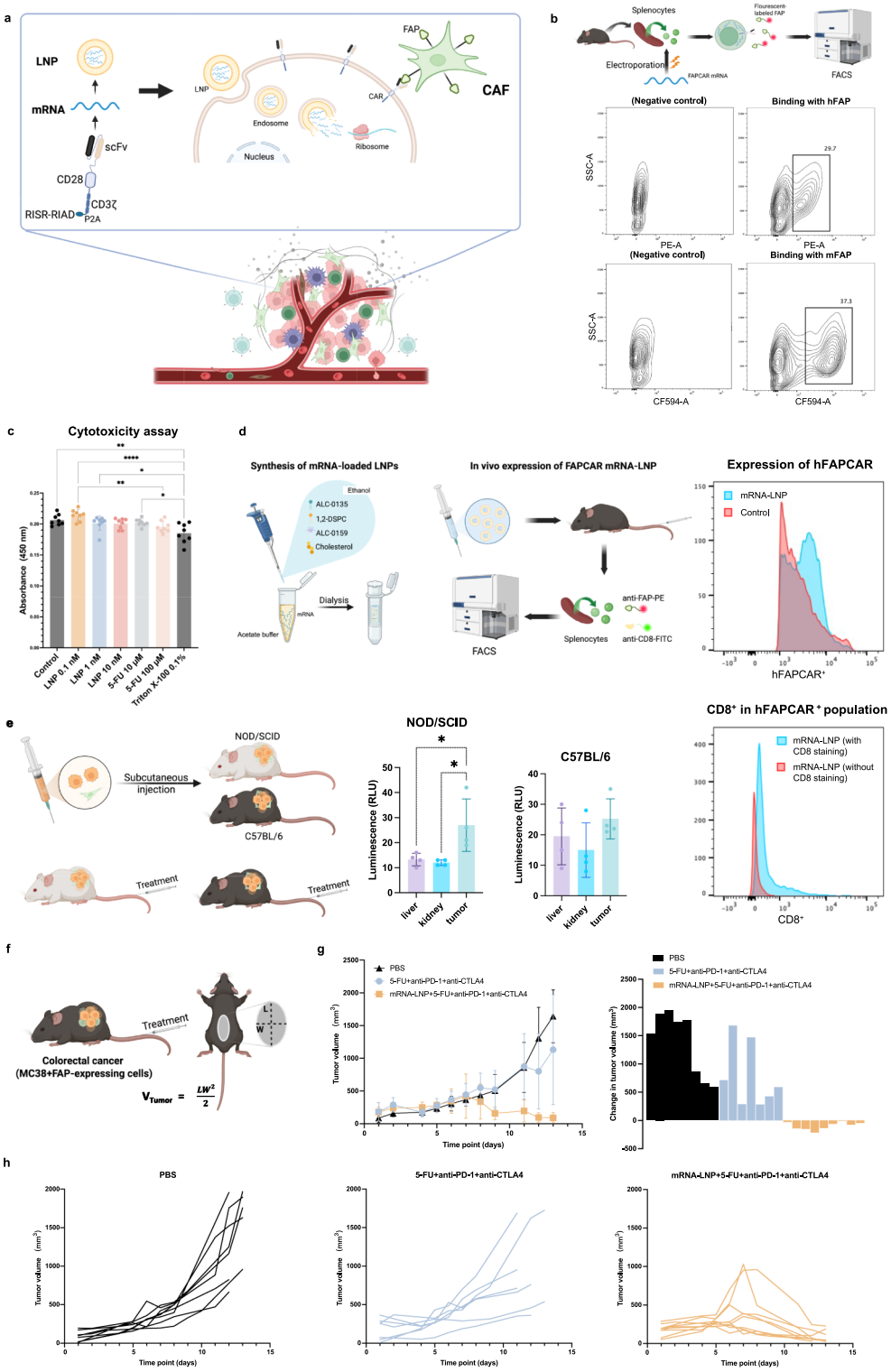
Sikun Meng[1], Tomoaki Hara[1], Tetsuya Sato[2], Shotaro Tatekawa[3], Yasuko Arao[1], Yoshiko Saito[1], Toshiro Hirai[4], Daisuke Motooka[5], Sarah Rennie[6], Taroh Satoh[7], Kazuhiko Ogawa[3], Yutaka Miura[8,9], Masaki Mori[10], Yuichiro Doki[7], Hidetoshi Eguchi[7] & Hideshi Ishii[1]✉

The therapeutic potential of chimeric antigen receptor (CAR) T-cell therapy in treating solid tumors is highly recognized, yet the complex and immunosuppressive nature of the tumor microenvironment, poor accessibility, and the instability of target antigens pose substantial challenges. Here, we present an mRNA-LNP-based therapeutic strategy that delivers mRNA encoding a fibroblast activation protein (FAP)-specific CAR to reprogram host immune cells in vivo and target cancer-associated fibroblasts within the tumor stroma. In multiple solid tumor mouse models, this approach, combined with chemotherapeutic agents and immune checkpoint inhibitors, achieved significant tumor regression and induced durable, antigen-specific immune memory. Incorporation of m^{6}A-modified CAR mRNA accelerated and amplified antitumor responses, while blockade of the macrophage migration inhibitory factor (MIF)-CD74 axis further improved tumor control by alleviating immune suppression. In patient-derived xenograft models, HOX family transcription factors were implicated in treatment resistance, highlighting a potential biomarker and therapeutic target. The evidence from this study demonstrates that targeting the tumor microenvironment with a controllable mRNA-modulated strategy achieves substantial antitumor efficacy and holds significant potential to enhance the applicability and acceptance of CAR-T cell therapy across a variety of cancers.

Keywords CAR-T therapy, mRNA, Solid tumor, Fibroblast activation protein, Tumor microenvironment

Cancer remains a significant global health challenge, among which solid tumors especially exemplify the conundrum[1,2]. The development of Chimeric Antigen Receptor T-cell (CAR-T) therapy has marked a significant advancement in oncology, showcasing notable achievement in treating certain hematological malignancies[3–5]. However, translating this to solid tumors has been met with limited efficacy, where the lack of stable antigens,

[1]Department of Medical Data Science, Center of Medical Innovation and Translational Research, Graduate School of Medicine, The University of Osaka, Yamadaoka 2-2, Suita, Osaka 565-0871, Japan. [2]Biomedical Research Center, Faculty of Medicine, Saitama Medical University, 1397-1 Yamane, Hidaka, Saitama 350-1241, Japan. [3]Department of Radiation Oncology, Graduate School of Medicine, The University of Osaka, Yamadaoka 2-2, Suita, Osaka 565-0871, Japan. [4]Vaccine Creation Group, BIKEN Innovative Vaccine Research Alliance Laboratories, Research Institute for Microbial Diseases, The University of Osaka, Yamadaoka 2-1, Suita, Osaka 565-0871, Japan. [5]Research Institute for Microbial Diseases, The University of Osaka, Yamadaoka 3-1, Suita, Osaka 565-0871, Japan. [6]Section for Computational and RNA Biology, Department of Biology, University of Copenhagen, DK2200 Copenhagen N Copenhagen, Denmark. [7]Department of Gastroenterological Surgery, Graduate School of Medicine, The University of Osaka, Yamadaoka 2-2, Suita, Osaka 565-0871, Japan. [8]Laboratory for Chemistry and Life Science, Institute of Integrated Research, Institute of Science Tokyo, 4259 Nagatsutacho, Midori-ku, Yokohama, Kanagawa 226-8501, Japan. [9]Department of Life Science and Technology, School of Life Science and Technology, Institute of Science Tokyo, 4259 Nagatsutacho, Midori-ku, Yokohama, Kanagawa 226-8501, Japan. [10]Tokai University Graduate School of Medicine, 143 Shimokasuya, Isehara, Kanagawa 259-1193, Japan. ✉email: hishii@gesurg.med.osaka-u.ac.jp



poor accessibility of the tumor, together with an intricate and immunosuppressive the tumor microenvironment (TME), stand as the three major obstacles complicating the dissection of CAR-T therapy's mechanisms and straightforward applications[6,7].

Shifting the focus towards the TME has become increasingly essential in cancer research, as it plays a crucial role in tumor progression and response to therapies[8–10]. Within the diverse components of the TME, cancer-associated fibroblasts (CAFs), emerge as key players, significantly driving tumor development and creating formidable physical and immunological barriers that hinder therapeutic interventions[11–13]. Fibroblast activation protein (FAP), highly expressed in CAFs and even directly in tumor cells in certain cancers, plays a critical role in this process, yet is rarely expressed in normal tissues[14,15]. Accumulating evidence shows that FAP is involved in both enzymatic and nonenzymatic activities that regulate tumor dynamics, including remodeling the extracellular matrix (ECM) and modulating immune responses[16–18].

◀**Fig 1**. Design and preclinical evaluation of mRNA-LNP-based FAP-targeted therapy in colorectal cancer models. (**a**) Schematic representation of the mRNA-LNP-based FAP-targeted CAR strategy. (**b**) In vitro binding assay of murine splenocytes transfected with human or mouse FAPCAR mRNA. (**c**) Cytotoxicity of mRNA-LNP to primary splenocytes. Cell viability was evaluated using a CCK-8 assay after 24 h exposure to mRNA-LNP or control reagents (n = 8 per group). Data are presented as mean ± SD. Statistical significance was determined by one-way ANOVA followed by Tukey's post hoc test. (**d**) In vivo validation of hFAPCAR mRNA-LNP expression. Splenocytes were collected 24 h after intravenous injection of hFAPCAR mRNA-LNP or PBS and analyzed by flow cytometry. PE-hFAP signal was compared between hFAPCAR- and control-treated mice, and $CD8^+$ staining was examined within the $hFAPCAR^+$ population (where the internal control was from the same treated mouse and stained only with PE-hFAP). (**e**) Biodistribution of FAPCAR-transfected splenocytes in immunodeficient (NOD/SCID) and immunocompetent (C57BL/6) models. Luminescence intensity was measured in biologically independent replicates (n=4), and statistical analysis between each tissue group was performed using one-way ANOVA with post hoc Tukey's test. Data are presented as mean ± SD. (**f**) Schematic representation of the experimental procedure. (**g**) Tumor growth and individual volume change in syngeneic colorectal cancer models. Error bars indicate mean ± SD (n=7-9). (**h**) Individual tumor growth curves.

In fact, the overexpression of FAP in CAFs, correlating with tumor invasiveness and poor prognoses, particularly in cancers with strong desmoplastic reactions, underscores the complex interplay between cancer cells and the TME[19]. The role of FAP extends to influencing tumor vasculature and immunosuppression, marking it as a potential factor in disrupting the TME and, when attacked, enhancing the infiltration and efficacy of immune cells, thereby transforming the TME into a more immune-responsive state[20,21] Moreover, the stability of FAP expression within the TME, compared to the variable expression of tumor-associated antigens on cancer cells, positions FAP as a strategic target for therapeutic intervention[22]. While most strategies directed at FAP, such as radiotherapy[23], tumor vaccines[24], and specific antibodies[25], are currently under early-stage investigation, their ability to transform the TME holds considerable promise for advancing cancer treatments[26,27]. In essence, focusing on CAFs and specifically targeting markers like FAP could provide strategically precise approach to overcome TME-related obstacles and boost the performance of cancer immunotherapies.

Lipid nanoparticles (LNPs) have emerged as a transformative platform for the delivery of mRNA therapeutics, exemplified by their critical role in the development of mRNA-based COVID-19 vaccines[28–30]. Beyond infectious diseases, mRNA-LNP technology is being actively explored in cancer immunotherapy, offering an alternative to traditional ex vivo cellular engineering approaches[31,32]. In particular, the in vivo delivery of mRNA encoding synthetic immune receptors, such as chimeric antigen receptors (CARs), enables transient reprogramming of host immune cells directly within the body[33,34]. This non-viral, transient approach reduces the risks associated with permanent gene integration, which have been linked to on-target, off-tumor toxicity and other adverse effects[35,36].

In this study, we developed an mRNA-LNP-based therapeutic strategy targeting FAP within the tumor stroma to reprogram host immune cells in vivo, thereby modulating the tumor microenvironment and elicit antitumor immunity (Fig. 1a). Unlike conventional CAR-T cell therapies, this approach does not require ex vivo cell manipulation or T cell-specific delivery, yet achieves potent tumor suppression and durable immune memory in multiple solid tumor models. Furthermore, we show that m^6A modification of the CAR mRNA enhances therapeutic efficacy, identify the MIF-CD74 axis as a potential barrier to response, and reveal HOX-driven transcriptional programs in patient-derived xenograft models as a potential resistance mechanism. These findings highlight a versatile and tractable immunotherapy platform that leverages stromal targeting, epitranscriptomic optimization, and host immunity to overcome key challenges in solid tumor treatment.

Results

FAP expression predicts malignancy in solid tumors

In our previous study, over 70 samples and more than 130,000 cells from six datasets were leveraged to establish a single-cell atlas of pancreatic ductal adenocarcinoma (PDAC), which identified different subtypes of CAFs. The interaction between these CAFs and malignant cells involves complex signaling pathways that promote tumor growth and maintenance, correlated with worse prognosis in PDAC patients due to their role in enhancing tumor growth and resistance to therapy[37]. We plotted the expression of FAP on the data, demonstrating that FAP is primarily expressed in CAFs and is present across almost all their subtypes (Fig. S1a). Besides, analysis based on Kaplan-Meier plotter and GEPIA (Gene Expression Profiling Interactive Analysis) revealed that increased FAP expression is highly correlated with malignant outcome in several solid tumors (Fig. S1b-c).

In vitro and in vivo evaluation of hFAPCAR expression and biodistribution

We synthesized mRNAs for the corresponding CARs against human FAP (hFAP) and mouse FAP (mFAP) in vitro and introduced the mRNAs into splenocytes collected from mouse spleens by electroporation. The Fluorescence-activated Cell Sorting (FACS) analysis demonstrated successful transfection and specific affinity of fluorescently labeled FAP proteins, where 29.7% and 37.3% of the splenocytes effectively expressed hFAPCAR and mFAPCAR mRNAs and bound to their corresponding FAPs in vitro, respectively (Fig. 1b). Subsequently, the synthesized mRNAs were encapsulated into lipid nanoparticles (physicochemical characterization summarized in Table S1). To assess the potential cytotoxicity of the mRNA-LNP formulation, primary mouse splenocytes were exposed to various concentrations of mRNA-LNP for 24 h and cell viability was measured (Fig. 1c). The absorbance values of splenocytes treated with mRNA-LNP at 0.1-10 nM were comparable to those of untreated

controls, whereas treatment with 5-fluorouracil (5-FU; 10 μM and 100 μM) or 0.1% Triton X-100 significantly reduced cell viability. These results demonstrate that the mRNA-LNP exhibits minimal cytotoxicity toward immune cells at the tested concentrations.

To examine whether mRNA-loaded lipid nanoparticles (mRNA-LNPs) could mediate CAR expression in vivo, splenocytes were collected 24 h after intravenous injection of hFAPCAR mRNA-LNPs or PBS and analyzed by flow cytometry. Under the same gating conditions (Fig. S2a), splenocytes from the mouse injected with hFAPCAR mRNA-LNPs showed a distinct positive peak in the PE-hFAP channel compared with the PBS control (Fig. 1d). In the same treated mouse, FITC-CD8 staining of PE-hFAP$^+$ cells revealed a clear CD8$^+$ population compared with the internal control, suggesting the expression of hFAPCAR in T cells (Fig. 1d). Based on these findings, we sought to investigate the systemic accumulation behavior in vivo.

To evaluate the in vivo biodistribution of FAPCAR-engineered splenocytes, mRNA encoding an mFAP-targeting CAR was co-transfected with NanoLuc luciferase mRNA to enable bioluminescence tracking. The transfected splenocytes were intravenously administered into both immunodeficient (NOD/SCID) and immunocompetent (C57BL/6) colorectal tumor models (Fig. 1e). In the NOD/SCID mice, which lack functional adaptive immunity, luminescence signals were predominantly detected in tumor tissues, with significantly lower intensities observed in the liver and kidneys. In contrast, in the immunocompetent C57BL/6 mice, luminescence in the tumor tissue was only marginally higher than in non-tumor tissues, with no statistically significant difference (Fig. 1e). These results suggest that the presence of an intact immune system may limit the accumulation or persistence of FAPCAR-expressing splenocytes at the tumor site.

mRNA-LNP-based FAPCAR therapy induces tumor regression and long-term immune memory

Next, we attempted to validate the efficacy of this therapeutic mRNA-driven FAPCAR approach in vivo (Fig. 1f). Considering the influence of the host immune system, we evaluated a combination treatment strategy involving mRNA-LNPs, immune checkpoint inhibitors (ICIs; anti-PD-1 and anti-CTLA-4 antibodies), and a chemotherapeutic agent.

We first tested this strategy in a colorectal tumor model using MC38 cells co-injected with FAP-expressing 3T3 cells at a ratio of 2:1. In this model, FAP-expressing stromal components accounted for one-third of the initial tumor cell population, mimicking a stromal-rich tumor microenvironment. As shown in Fig. 1g-h, tumor growth in the group treated with mRNA-LNPs in combination with 5-FU and ICIs was noticeably suppressed compared to the PBS control group and the group treated with 5-FU plus ICIs alone. The individual tumor growth curves also reflected this trend, with most tumors in the mRNA-LNP-treated group exhibiting stable or regressing volumes over the observation period. Fluorescence imaging of tumor sections from the mRNA-LNP-treated mice showed detectable labeled FAP protein, suggesting local FAPCAR expression within the tumor tissue (Fig. S2b). To further explore the applicability of this treatment strategy across tumor types, we applied the same combination therapy to additional solid tumor models established with 4T1 (triple-negative breast cancer, TNBC), E0771 (HER2-positive breast cancer), and Renca (renal carcinoma) cells, each co-injected with FAP-expressing 3T3 cells at a 2:1 ratio. As shown in Supplementary Fig. S2c-e, all three models exhibited a similar trend: tumor growth was significantly restrained in the group treated with mRNA-LNPs in combination with chemotherapeutic agents and ICIs.

The establishment of immune memory is crucial for ensuring long-term protection against cancer recurrence. To assess whether immune memory had been established, we rechallenged the colorectal cancer and TNBC models previously cured by the combination therapy (mRNA-LNPs, chemotherapeutic agents, and ICIs), with homologous and heterologous tumors, without administering further treatment. In the first round of rechallenge for colorectal cancer models, tumors derived from MC38 and E0771 cells were implanted into the dorsal and mammary fat pad regions, respectively. The results showed that the homologous MC38-derived tumors were completely rejected, while the heterologous E0771-derived tumors grew progressively (Fig. S2f). In a second round of rechallenge, MC38 cells were transplanted into the mammary fat pad, and tumor growth was again effectively suppressed (Fig. S2f). A similar pattern was observed in the TNBC models, where the homologous 4T1-derived tumors were significantly suppressed compared to the heterologous MC38-derived tumors (Fig. S2g). This pattern of tumor rejection suggests the establishment of antigen-specific immune memory, which may contribute to long-term tumor control. Interestingly, when we administered anti-CD8α (to deplete CD8$^+$ T cells) or FTY720 (to prevent T cell egress from lymphoid tissues) in the rechallenged colorectal cancer models, the tumor grew rapidly in the mouse treated with anti-CD8α, while the tumor in the mouse treated with FTY720 showed a gradual regression, albeit at a slower pace compared to the control treated with PBS (Fig. S2h). The observation that immune memory remained effective even when T cells were confined to lymphoid tissues (by FTY720) suggests that non-circulating, tissue-resident memory T cells (Trm) played a key role in mediating tumor control.

Insights into optimizing the antitumor efficacy

Although the mRNA-LNP-based FAP-targeted therapy achieved effective tumor suppression, variability in tumor responses still requires further optimization. Below, we present preliminary findings that suggest potential avenues to enhance antitumor efficacy in future applications.

N6-Methyladenosine (m^{6}A) modification enhanced the anti-tumor efficacy

N6-methyladenosine (m^{6}A) modification is major epitranscriptomic mark that involves the addition of a methyl group to the adenosine base of an RNA molecule. This modification is known to regulate RNA stability, translational efficiency and cellular localization[38]. We have recently confirmed that m^{6}A modifications can alter gene expression[39]. Based on these proven advantages, we applied m^{6}A modification on the therapeutic mRNA

and evaluated its impact in the syngeneic colorectal tumor models (Fig. 2a). As a result, the m^{6}A modification was demonstrated to accelerate the anti-tumor effect (Fig. 2b-c). Bar graph of tumor volume changes further confirmed the superior antitumor effect of m^{6}A-modified mRNA-LNPs (Fig. 2c), suggesting a more consistent and potent therapeutic effect conferred by m^{6}A-modified transcripts.

MIF-CD74 limited the anti-tumor efficacy

Although the mRNA-based therapy combined with chemotherapeutic agents and ICIs successfully eradicated tumors in some syngeneic models, incomplete responses or relapses were still observed in certain mice. To investigate mechanisms associated with limited therapeutic efficacy, we performed single-cell RNA sequencing (scRNA-seq) on untreated and post-treatment relapsed tumor tissues from the MC38 model, which share the common phenotype of persistent tumor burden (Fig. 2d). UMAP analysis revealed heterogeneous cellular compositions, including abundant macrophages and CAFs. Notably, we observed high expression levels of macrophage migration inhibitory factor (MIF) and CD74 in these tissues (Fig. 2e). Recent multi-omics analyses in neuroblastoma have identified MIF as a tumor-derived, abundantly secreted factor that directly impairs CAR T-cell activation and cytotoxicity via CD74 engagement[40]. To further dissect intercellular signaling dynamics, we performed ligand-receptor interaction analysis, which highlighted MIF-CD74 as one of the dominant outgoing and incoming signaling axes between macrophages, CAFs, and cancer cells (Fig. 2f). Although relapsed and untreated tumors are not biologically identical, their inclusion aimed to capture common immune features associated with incomplete tumor clearance, suggesting that the MIF-CD74 axis may contribute by fostering an immunosuppressive microenvironment. To test the functional contribution of this pathway, we incorporated neutralizing antibodies against MIF and/or CD74 into the m^{6}A-mRNA-LNP treatment regimen. Tumor volume analysis demonstrated that blockade of either MIF or CD74 improved tumor control, while simultaneous inhibition of both ligands and receptors led to the most pronounced tumor suppression (Fig. 2g).

Translational relevance and potential resistance mechanisms revealed by patient-derived xenograft (PDX) models

To extend our findings toward clinical relevance and explore potential mechanisms underlying variable therapeutic responses, we employed patient-derived xenograft (PDX) models of colorectal cancer. CAR-T cells that overexpress 7SL1 RNA, a component of the signal recognition particle (SRP), have been reported to release 7SL1 RNA as extracellular vesicles (EVs), thereby activating other immune cells and enhancing their own expansion, persistence, and resistance to exhaustion[41]. Based on these observations, we sought to investigate how the presence of immune cells expressing 7SL1-like RNA might influence the therapeutic efficacy of the mRNA-LNP therapy. To this end, we generated transgenic mice constitutively expressing GFP-tagged 7SL1-like RNA under the control of the CAG promoter and used splenocytes from these mice for adoptive transfer. We established two PDX models, PDX-1 and PDX-2, which were derived from tumor tissues of two individual colorectal cancer patients. For treatment, splenocytes from 7SL1 knock-in mice were co-administered with mRNA-LNPs in the PDX-1 model, whereas both 7SL1 and wild-type splenocytes were used in the PDX-2 model, as illustrated in Fig. 3a. In the PDX-1 model, tumor growth was markedly suppressed in the treatment group (Fig. 3b). In the PDX-2 model, both treatment groups exhibited a suppressive effect on tumor growth, with the group receiving 7SL1 splenocytes a comparable inhibitory trend (Fig. 3c). To investigate the gene expression profiles of tumors under each treatment condition, we harvested tumors after therapy and performed RNA sequencing (RNA-seq). Gene set enrichment (GSE) analysis revealed that, compared to the PBS control group, the combination of mRNA-LNP administration and 7SL1-expressing immune cells led to a downregulation of pathways such as negative regulation of developmental process, tube morphogenesis, and blood vessel development in the PDX-1 model, whereas lymphocyte migration and inflammatory response were upregulated in the PDX-2 model (Fig. 3d and f). In addition, in PDX-2 tumors treated with wild-type splenocytes and mRNA-LNP, we observed increased expression of genes involved in T cell migration, interleukin-10 production, and inflammatory response (Fig. 3e). These results indicate that immune cells expressing 7SL1-like RNA exhibited antitumor and transcriptional response patterns comparable to those of wild-type immune cells, highlighting a potential role of 7SL1 in modulating mRNA-LNP-mediated therapeutic outcomes.

Although the antitumor effect was less pronounced in PDX-2 compared to PDX-1, we sought to identify gene expression differences that may explain this discrepancy. Comparative transcriptomic analysis of PDX-2 and PDX-1 tumors treated with mRNA-LNP and 7SL1-expressing splenocytes revealed that embryonic skeletal system morphogenesis and development pathways were upregulated in the treatment-resistant PDX-2 model (Fig. 3g). To explore which transcription factors were activated in each condition, we performed ChIP-X Enrichment Analysis 3 (ChEA3) using the top-ranked differentially expressed genes (DEGs). In the treatment-resistant PDX-2 model, transcription factors belonging to the HOX family were enriched among the top 100, 20, and 10 DEGs (Fig. S3a). In contrast, the HOX family transcription factors were not detected in the PDX-1 model under the same treatment conditions (Fig. S3b), nor were they observed when comparing untreated tumors between PDX-1 and PDX-2 (Fig. S3c). These findings suggest that the treatment-resistant PDX-2 model might alter its gene expression program in response to mRNA-LNP and 7SL1-expressing splenocyte therapy through activation of HOX family transcription factors, a feature not observed in the treatment-sensitive PDX-1 model.

To investigate whether the therapeutic effect was associated with changes in chromatin structure, we performed assay for transposase-accessible chromatin using sequencing (ATAC-seq). Analysis of open chromatin regions revealed that in both control and treated PDX-1 tumors, approximately 9% of the accessible regions were located in promoter regions and about 44% in distal intergenic regions, with similar distributions across other genomic elements. In contrast, in the PDX-2 tumors treated with mRNA-LNP and 7SL1-expressing splenocytes, the proportion of promoter-associated accessible regions increased to approximately 25%, while distal intergenic regions decreased to about 37% (Fig. 4a). Chromosome-wide peak distribution analysis revealed

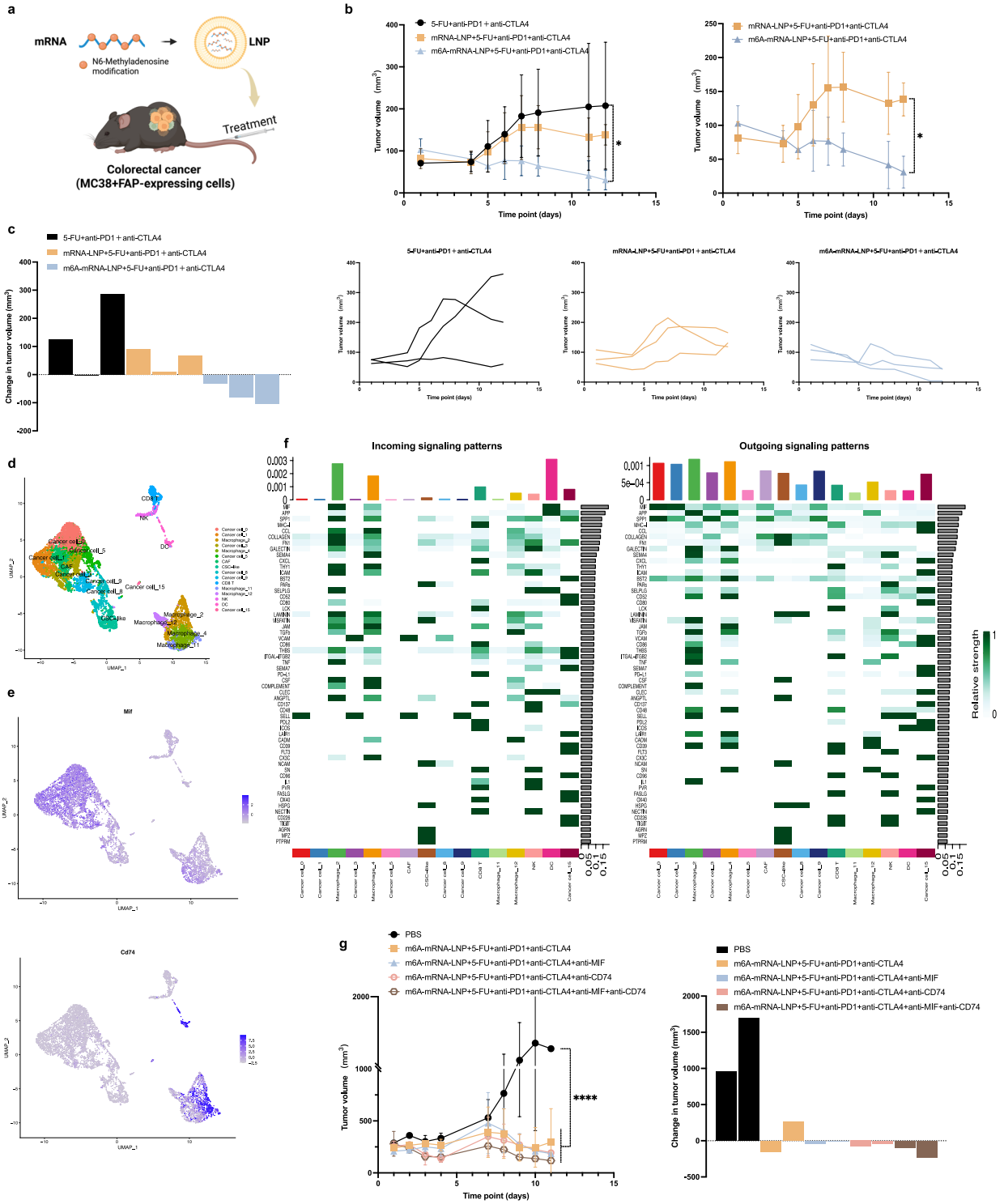


Fig 2. Optimizing antitumor efficacy via m^{6}A modification and MIF–CD74 axis blockade. (**a**) Schematic overview of the experimental design, which was created with BioRender.com. (**b**) Tumor growth in syngeneic colorectal cancer models to assess m^{6}A modification effects. Statistical analysis was conducted using two-way ANOVA with Tukey's post hoc test (left) and Bonferroni's post hoc test (right). Data are presented as mean ± SD (n=3). (**c**) Individual volume change and tumor growth curves. (**d**) UMAP plot of the single-cell RNA sequencing (scRNA-seq) data on untreated and post-treatment relapsed tumor tissues. (**e**) Feature plots of MIF and CD74 in scRNA-seq. (**f**) CellChat analysis of MIF-CD74 axis communication. The heatmap shows incoming and outgoing MIF signal patterns across cell clusters. (**g**) Tumor growth and individual volume change in syngeneic colorectal cancer models to assess MIF-CD74 blockade. Statistical analysis was conducted using two-way ANOVA with Tukey's post hoc test. Error bars indicate mean ± SD (n=2).

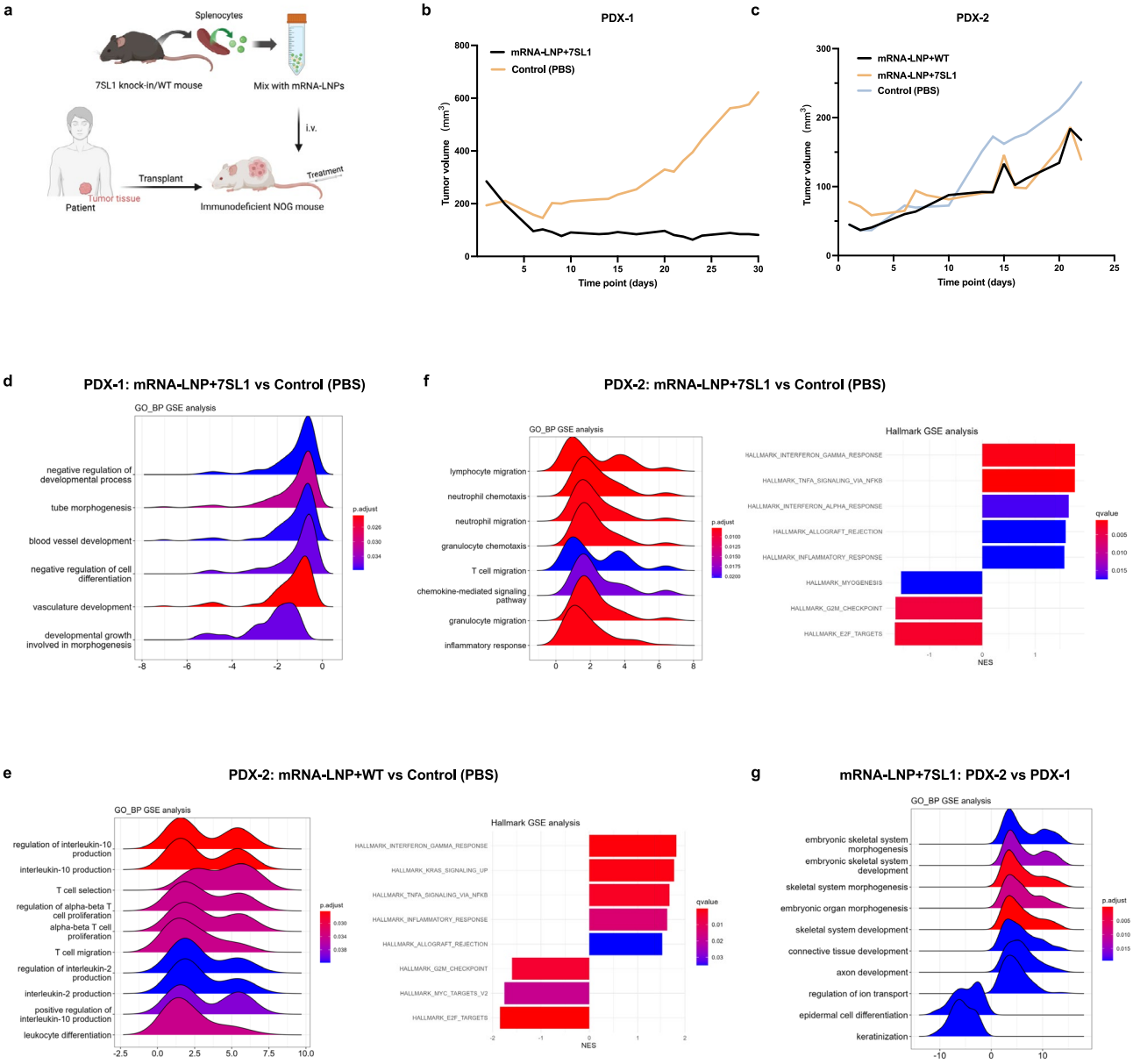


Fig 3. mRNA-LNP exerts anti-tumor effects in PDX models. (**a**) Schematic overview of the experimental design, which was created with BioRender.com. (**b**) Individual tumor growth curves in PDX-1. (**c**) Individual tumor growth curves in PDX-2. (**d**) GSE analysis in PDX-1. Gene ontology (GO) terms enriched in the group treated with 7SL1-like RNA-expressing immune cells and mRNA-LNP compared to the PBS control. (**e**) GSE analysis in PDX-2. GO terms and Hallmark gene sets enriched in the group treated with 7SL1-like RNA-expressing immune cells and mRNA-LNP compared to the PBS control. (**f**) GSE analysis in PDX-2. GO terms and Hallmark gene sets enriched in the group treated with wild-type immune cells and mRNA-LNP compared to the PBS control. (**g**) Comparative GSE analysis between PDX-1 and PDX-2 treated with 7SL1-like RNA-expressing immune cells and mRNA-LNP.

distinct alterations in chromatin accessibility across chromosomes in each tumor type (Fig. 4b). Furthermore, peak density near transcription start sites (TSS) was markedly higher in the PDX-2 tumors treated with mRNA-LNP and 7SL1 splenocytes compared to other groups (Fig. 4c). However, the read count frequency around TSS regions remained similar among all conditions (Fig. 4d). In the mRNA-LNP and 7SL1 splenocyte-treated group, PDX-2 tumors showed markedly greater ATAC-seq signal intensity at HOX gene clusters, as well as at GRAMD1A and CTSC, compared to PDX-1 (Fig. S4). These findings suggest that chromatin remodeling in treatment-resistant tumors may contribute to altered gene expression patterns, thereby playing a role in the resistance to mRNA-LNP and 7SL1 splenocyte-based therapy.

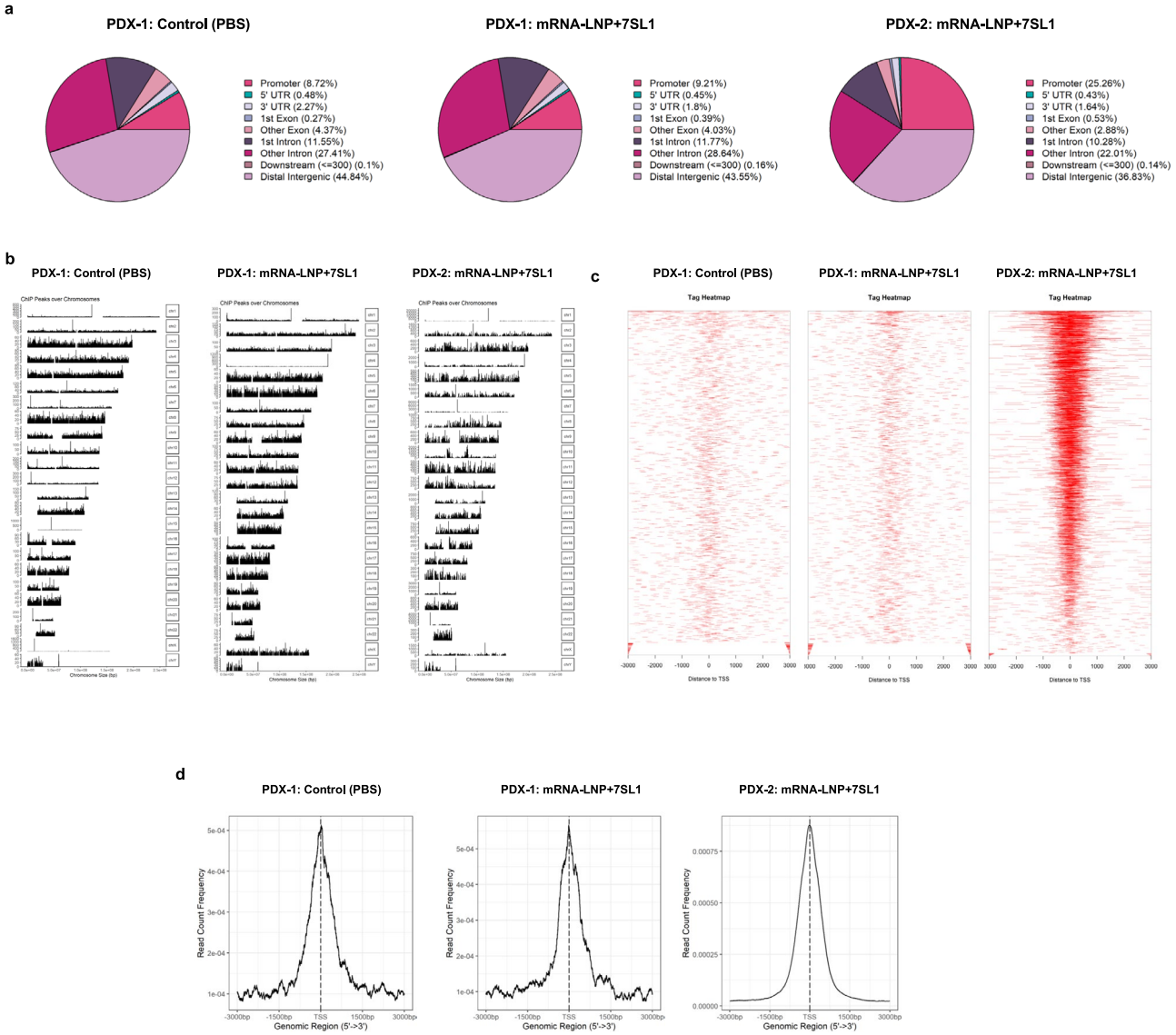


Fig 4. PDX-2 exhibits chromatin structure modulation compared to control and PDX-1. (**a**) Genomic distribution and proportions of ATAC-seq peaks. (**b**) Chromosomal distribution of ATAC-seq peaks. (**c**) Tag heatmap of peaks around transcription start sites (TSS). (**d**) Read count frequency around TSS regions.

Discussion

CAR-T cell therapy has revolutionized the treatment of several hematological malignancies, capturing the interest of an increasing number of scientists who are striving to harness its potential for solid cancers[42–44]. Based on previous attempts to overcome the immunosuppressive tumor microenvironment and improve T cell trafficking into solid tumors[45,46], our strategy is to utilize mRNA-LNP-based therapy to target the TME via FAP. A recent study by Rurik et al. demonstrated a pioneering approach to generate anti-fibrotic CAR T cells in vivo using CD5-targeted LNPs carrying FAPCAR mRNA, which transiently reprogrammed T cells to reverse cardiac fibrosis[33]. The present study extends this concept to solid tumor immunotherapy, employing untargeted mRNA-LNPs to deliver FAPCAR mRNA systemically. With the assistance of chemotherapeutic agents and immune checkpoint inhibitors, the mRNA-LNP-based FAP-targeted strategy elicited pronounced tumor regression in multiple syngeneic solid tumor models, and subsequently established antigen-specific long-term immune memory, which provides a practical and broadly applicable framework for CAR-T therapy against solid tumors. Compared with conventional adoptive cell therapies, the mRNA-based approach eliminates the need for ex vivo genome editing and permanent genetic modification, enabling flexible control over the timing and dosage of CAR expression through repeated dosing, as demonstrated in the in vivo experiments, offering a safer and more controllable alternative to conventional CAR-T strategies.

Although our approach involved systemic administration of mRNA-LNPs without cell-type-specific targeting, the observed antitumor efficacy demonstrates that effective CAR-T cell activity can be elicited even in the absence of selective T cell transfection. The CAR construct was specifically designed for T cell function,

incorporating a CD8α leader and hinge region together with CD28 and CD3ζ intracellular domains, which require T cell-specific signaling machinery to operate effectively[47]. Therefore, despite potential transfection of non-T cell subsets such as NK cells, B cells, or macrophages, the therapeutic effect is most likely mediated by CAR-T cells selectively activated through these T cell-restricted signaling pathways.

Notably, while many recent mRNA-CAR studies have employed ligand-modified LNPs for targeted delivery[33,35,48], our results demonstrate that untargeted LNPs can also trigger robust in vivo antitumor effects. Besides the permeability and retention (EPR) effect, where the abnormal vasculature of solid tumors permits nanoparticle entry into the tumor interstitium and inadequate lymphatic drainage promotes their retention[49], several alternative pathways have recently been proposed that may also facilitate nanoparticle delivery. These include active transcytosis across tumor endothelium, immune cell-mediated transport, and vascular targeting followed by rapid drug release, all of which could contribute to effective accumulation and penetration in the tumor microenvironment[50]. In addition, the ability of mRNA-LNPs to control the timing and dosage of CAR expression may contribute to therapeutic efficacy by maximizing functional CAR-T cell activity during peak expression windows. These findings suggest that non-targeted LNPs remain a viable option and could pave the way for future innovations in organ- or microenvironment-targeted delivery systems.

We conducted in vivo experiments using syngeneic models to capture the interplay between tumor, treatment, and immunity. Tumor cells in solid tumors are typically heterogeneous and become highly unstable due to immune editing, with CAR-T cells potentially adding to this selective pressure[51,52]. Given that CAR-T cells are designed to target specific antigens, inducing bystander effects, where CAR-T cells promote the killing of non-target cells during lysis of target cells, may be a promising approach for solid tumor therapy[53,54]. Epitope spreading, in which the immune response expands from the initial antigen epitope to additional epitopes on the same or different antigens, is considered an efficient mechanism for such bystander effects[53]. In our in vivo experiments, the mRNA-LNP-based therapy targeting only FAP achieved profound and sustained tumor regression and resistance to rechallenge, possibly by eliminating FAP^+ CAFs to remodel the immunosuppressive tumor microenvironment, and release tumor-associated antigens that promote epitope spreading to enable the clearance of cancer cells lacking the CAR target. This protective immunity may also involve tissue-resident memory T cells (Trm), which mediate rapid local immune responses and contribute to long-term immunological memory[55,56]. In our single-cell analysis, $CD8^+CD69^+$ clusters in untreated and post-treatment relapsed tumors showed low CD103 expression (Fig. S2i), a phenotype associated with T cell exhaustion rather than effective Trm cells[57], potentially contributing to uncontrollable growth. Maximizing the presence and function of effective Trm populations could further strengthen durable tumor control.

In the preliminary exploration, incorporating m^6A modification into the therapeutic mRNA resulted in a faster and stronger antitumor response. The potential mechanism involves m^6A marks being recognized by binding proteins such as YTHDF2, which stabilize mRNA and delay its degradation[58], as well as YTHDF1 and IGF2BP family proteins, which enhance translational efficiency[59,60]. In addition, m^6A modification can reduce the innate immunogenicity of mRNA[61], helping to balance immune activation. Sustained CAR expression may provide prolonged antigen stimulation, increasing the likelihood of epitope spreading and promoting a durable immune response.

Homeobox (HOX) genes encode transcription factors that play critical roles in embryonic development, particularly in anterior-posterior patterning and organogenesis. In adult tissues, HOX gene expression is typically silenced or tightly regulated; however, accumulating evidence suggests that dysregulation of HOX genes is a hallmark of various cancers, where they contribute to tumor initiation, progression, and therapeutic resistance[62]. For instance, overexpression of HOXA9 and HOXA10 has been implicated in the pathogenesis and poor prognosis of Acute myeloid leukemia (AML)[63,64]. In lung cancers with KRAS mutations, HOX gene activation forms part of an epigenetically deregulated axis that confers vulnerability to chromatin-modifying therapies[65]. In this study, PDX-2, which exhibited resistance to treatment, showed modulation of gene expression driven by HOX family transcription factors. These findings suggest that the efficacy of FAP-targeted mRNA-LNP therapy might be attenuated in tumors with high HOX gene expression. While CAR-T cell therapy can also demonstrate limited efficacy in certain cases[66], the combination of mRNA-LNP treatment with anti-tumor agents targeting HOX family genes might help restore therapeutic response. Furthermore, from the perspective of predicting treatment efficacy, evaluating HOX gene expression levels prior to mRNA-LNP therapy might serve as a useful biomarker.

In summary, our findings provide proof-of-concept that FAP-targeted CAR expression via mRNA-LNP delivery can effectively induce durable antitumor immunity. Despite these advances, the approach currently relies on combination with chemotherapeutic agents and immune checkpoint inhibitors, and its efficacy across broader tumor contexts remains to be determined. Future work should focus on optimizing delivery systems and mRNA modifications, elucidating resistance mechanisms such as HOX-driven transcriptional and epigenetic reprogramming, and expanding preclinical validation in diverse PDX and organoid models to accelerate clinical translation.

This study has several limitations. First, systemic toxicity of FAPCAR mRNA-LNP was not comprehensively assessed. Although in vitro assays using primary splenocytes showed minimal cytotoxicity, further studies are required to define the safety profile and therapeutic window of this platform. Second, it should be acknowledged that the biodistribution and tumor accumulation of the mRNA-LNPs themselves were not comprehensively analyzed in this study. The preliminary fluorescence observations provide only qualitative evidence, and more systematic biodistribution analyses are planned for future work. Finally, several exploratory or supplementary assays were performed with smaller sample sizes, which may limit the statistical power of some comparisons. Future studies with larger cohorts and extended observation periods will be important to further validate the reproducibility and long-term safety of this mRNA-LNP-based therapeutic approach.

Materials and methods

Analysis on the effect of FAP expression in solid cancers

In this study, we employed Kaplan-Meier plotter (https://kmplot.com/analysis/) and GEPIA (http://gepia.cancer-pku.cn) for a comprehensive analysis to investigate the impact of high versus low expression of FAP on overall survival (OS) in various solid tumors. The Kaplan-Meier plotter, a statistical tool, was used to generate survival curves, illustrating the probability of survival over time among different patient cohorts based on FAP expression levels. GEPIA, an online platform for cancer and normal gene expression profiling, was utilized to further validate and refine these findings by correlating FAP expression with clinical outcomes. This comprehensive approach leverages the robust capabilities of these tools to elucidate the role of FAP in cancer progression.

Synthesis of mRNA-loaded lipid nanoparticles (LNPs)

All plasmid vectors were custom-designed and provided by GenScript Biotech Corp. (Piscataway, NJ, USA). These plasmids were used as templates for in vitro transcription of the therapeutic mRNA. The CAR construct encoded by the therapeutic mRNA comprised the following elements in sequence: a T7 promoter, 5′ untranslated region (UTR), a CD8α leader peptide, FAP-targeting scFv (VH–VL), a CD8α hinge region, intracellular signaling domains from mouse CD28 and CD3ζ, and a P2A sequence enabling co-expression of an RISR–RIAD domain. All components were codon-optimized for murine expression. For amplification, the plasmids were transformed into E. coli (Thermo Fisher Scientific, Waltham, MA, USA; Cat.# C404010) and isolated using the Plasmid Midi Kit (QIAGEN, Hilden, Germany; Cat.# 12145). Subsequently, the plasmids were digested with Hind III (Nippon Gene Co., Ltd., Tokyo, Japan; Cat# 311-01163) to produce linear DNA, which was further purified through ethanol precipitation. Finally, the target gene fragments were transcribed into FAPCAR mRNA using the Takara IVTpro™ T7 mRNA Synthesis System (Takara Bio Inc., Shiga, Japan; Cat# 6144) , along with CleanCap Reagent AG (TriLink, San Diego, CA, USA; Cat# N-7113) and N1-Methylpseudouridine-5'-Triphosphate (TriLink, Cat# N-1081). The LNPs containing the mRNA were manipulated using Lipid Nanoparticle (LNP-0315) Exploration Kit (Cayman Chemical, Ann Arbor, MI, USA; Cat# 36426) according to the manufacturer's instruction. The LNPs encapsulating mRNA were prepared using the Lipid Nanoparticle Exploration Kit (LNP-0315; Cayman Chemical, Ann Arbor, MI, USA; Cat. #36426) according to the manufacturer's protocol. Briefly, ionizable lipid ALC-0315, 1,2-distearoyl-sn-glycero-3-phosphocholine (DSPC), cholesterol, and PEG-lipid ALC-0159 were dissolved in ethanol at a molar ratio of 46.3 : 9.4 : 42.7 : 1.6. The lipid mixture was rapidly combined with an aqueous mRNA solution in 50 mM sodium acetate at an ethanol : aqueous ratio of 1 : 3, a lipid : oligonucleotide (w : w) ratio of 10:1. The N:P ratio (molar ratio of lipid amine groups to mRNA phosphate groups) was maintained at 3 : 1. The formulated mRNA-LNPs were dialyzed against PBS overnight at 4 °C using VivaSpin 500 centrifugal filters (MWCO 50 kDa, Sartorius, Cat. # VS0131).

Cell lines

Laboratory generation of FAP-expressed cells

NIH/3T3 cells (Clontech, Shiga, Japan; Cat.# 631198) stably expressing the Tet-On 3G transactivator were used for inducible gene expression. A codon-optimized mouse FAP gene, fused at the C-terminus with a 3×FLAG tag (GenScript), was inserted downstream of the IRES2 sequence in the pTRE-Dual2 vector (Clontech, PT5038-5), enabling doxycycline-inducible bicistronic expression of mCherry and FAP. The final construct was linearized using PvuI (Takara Bio Inc., Cat.# 1242A) and transfected into the NIH/3T3-Tet-On cells via electroporation.

The cells were plated in 10-cm dishes and cultured in Dulbecco's Modified Eagle Medium (DMEM; Nacalai Tesque, Inc., Kyoto, Japan; Cat# 08456-36) supplemented with 1 μg/mL doxycycline (Dox) and Tet-approved fetal bovine serum (FBS; Clontech, Cat.# 631105) for 24 hours. Then the cells were trypsinized (Nacalai Tesque, Inc., Cat.# 35555-54) and suspended in Hank's Balanced Salt Solution (HBSS, Thermo Fisher Scientific, Cat.# 14025) to make a cell sorting solution. By using fluorescence-activated cell sorting (FACS, BD FACSymphony S6, Becton, Dickinson and Company, East Rutherford, NJ, USA), mCherry-positive (indicative of successful FAP induction) cells were selected and collected, which were subsequently stored in Cellbanker 1 (Nippon Zenyaku Kogyo Co., Ltd., Fukushima, Japan; Cat# CB011) to be deployed as FAP-expressed cells in the following experiments.

When used, the cells were thawed and cultured in DMEM with 10% heat-inactivated (56 °C, 30 min) FBS (Cosmo Bio Co., Ltd., Tokyo, Japan; Cat.# 04-007-1A), at 37°C and 5% CO_2.

Cancer cell lines

MC38 cell line (Applied Biological Materials Inc., Richmond, BC, Canada; Cat.# T8291), 4T1-Luc cell line (National Institutes of Biomedical Innovation, Health and Nutrition, Osaka, Japan; JCRB1447), E0771 cell line (CH3 BioSystems, Buffalo, NY, USA; Cat.# 94A001) and Renca cell line (American Type Culture Collection, Manassas, VA, USA; Cat.# CRL-2947) were used for colorectal cancer, triple-negative breast cancer (TNBC), medullary breast adenocarcinoma and renal cancer, respectively. The cells were thawed and cultured in a suitable medium at 37°C and 5% CO_2. The medium for MC38 contained DMEM with 10% heat-inactivated FBS and PreGrow III Medium (Applied Biological Materials Inc., Cat.# TM003) with 10% FBS and 1% Penicillin/Streptomycin Solution (Applied Biological Materials, Cat.# G255), at a ratio of 1:1. The medium for 4T1 and E0771 was DMEM with 10% heat-inactivated FBS. The medium for Renca was RPMI 1640 (Nacalai Tesque, Inc., Cat# 30264-56) with 10% heat-inactivated FBS.

Mice

All animals in this study were cared according to Osaka University's standards for care and use of laboratory animals, and operation procedures were performed in accordance with protocols approved by the Laboratory Investigation Committee, Osaka University Medical School (Approval No. 04-105-014). The study is reported

in accordance with the ARRIVE guidelines. The mice were maintained in a specific pathogen-free facility under controlled environmental conditions (23°C±1.5°C, 45%±15% humidity, 12-hour light/dark cycle) with free access to autoclaved food and water. Health status was monitored daily by trained veterinary staff following institutional guidelines. Generation of 7SL1-like RNA-expressing mice was outsourced to the animal experimentation facility at Osaka University. The 7SL1-like RNA sequence was designed by replacing the AcGFP1 gene with the RN7SL1 sequence "ATGCCGATCGGGTGTCCGCACTAA." A DNA construct containing the 7SL1-like RNA sequence under the control of the CAG promoter at the 5' end was inserted into the mouse genome immediately upstream of the endogenous RN7SL1 gene locus using CRISPR-Cas9 technology.

Establishment of cell line-derived tumor models and patient-derived xenograft (PDX) models

Cell line-derived tumor models were established in both immunocompetent and immunodeficient mice. In immunocompetent C57BL/6 mice (Japan SLC Inc., C57BL/6JmsSlc), syngeneic models were generated by subcutaneous injection of a cell mixture containing 5*10^6 cancer cells (from the MC38, Renca, E0771, or 4T1 cell lines) and 2.5*10^6 cancer FAP-expressing 3T3 cells (2:1 ratio). For biodistribution analysis, immunodeficient models were additionally established in NOD/SCID mice (CLEA Japan, Inc.) using MC38 cancer cells and FAP-expressing 3T3 cells, following the same injection protocol.

In all cases, cells were harvested and resuspended in DMEM supplemented with 10% FBS. The suspension was kept on ice and mixed with 10% Corning® Matrigel® Growth Factor Reduced (GFR) Basement Membrane Matrix (Corning Inc., Somerville, MA, USA; Cat.# 354230) and 10% doxycycline (final concentration: 1 μg/mL) to support tumor growth and doxycycline-inducible FAP expression in 3T3 cells. The colorectal and renal tumors were injected in the back subcutaneously and the breast tumors were in the mammary fat pad of respective mice background.

PDX models were established by subcutaneously transplanting colorectal cancer tissues, which were obtained from two certain clinical patients (referred as PDX-1 and PDX-2), into immunodeficient NOG mice (CLEA Japan, Inc., NOD/Shi-scid, IL-2RγKO). The tumor tissues used for PDX establishment were purchased from the Central Institute for Experimental Medicine and Life Science. The institute confirmed that all human samples were collected with informed consent from donors and with approval from the appropriate institutional ethics committee, in compliance with all relevant guidelines and regulations. In detail, the tissues were thawed in a 37°C water bath, cut into 2–3 mm pieces, and suspended in a 2:1 mixture of Matrigel and RPMI-1640 medium with 10% FBS, and maintained on ice. Mice were anesthetized using a combination of three anesthetic agents, and the dorsal skin was shaved and incised. Subsequently, 2–3 tumor pieces were implanted subcutaneously into each mouse, and the incision was closed using SurgiBond (Bydand Medical, NSW, Australia).

In vitro assessment of FAP binding by FAPCAR-engineered splenocytes

Splenocytes were obtained from the spleen of a 5-week-old male mouse maintained in accordance with Osaka University's institutional guidelines for laboratory animal care. All procedures were approved by the Laboratory Investigation Committee, Osaka University Medical School. The spleen was minced in cold DMEM supplemented with 10% FBS and filtered through a 40 μm cell strainer. The cell suspension was centrifuged at 380 × g for 5 minutes at 4°C, and red blood cells were lysed using ACK lysis buffer (Thermo Fisher Scientific, Cat.# A1049201). After washing for twice, the cells were resuspended in Opti-MEM (Thermo Fisher Scientific, Cat.# 31985062) for mRNA transfection. Splenocytes were divided into three groups (2.5*10^7 cells per group): one group was electroporated with 10 μg of synthesized human FAPCAR mRNA, another with 10 μg of mouse FAPCAR mRNA, and the third group received no electroporation as a negative control. Electroporation was performed in 2 mm cuvettes using the NEPA21 Super Electroporator Type II (Nepa Gene Co., Ltd., Chiba, Japan), following the manufacturer's protocol. Following electroporation, cells were cultured in DMEM supplemented with 10% FBS and 100 ng/mL IL-2 (Thermo Fisher Scientific, Cat.# 200-02) for 24 hours at 37°C in 5% CO_2. Cells transfected with human FAPCAR mRNA were incubated with PE-labeled human FAP protein (Acro Biosystems, Newark, DE, USA; Cat.# FAP-HP245), while those transfected with mouse FAPCAR mRNA were stained with mouse FAP protein tagged with a His-tag (Acro Biosystems, Cat.# FAP-M52H3), followed by secondary labeling with Alexa Fluor 594-conjugated anti-His antibody (Medical & Biological Laboratories, Tokyo, Japan; Cat.# D291-A59). After washing and centrifugation, cells were resuspended in PBS and analyzed by FACS using a BD FACSymphony S6 (Becton, Dickinson and Company). Flow cytometric data were processed using FlowJo v10.8.1.

Cytotoxicity assay and in vivo validation of hFAPCAR expression via mRNA-LNP delivery

To evaluate the cytotoxicity of mRNA-LNP, freshly isolated mouse splenocytes were seeded in 96-well plates at a density of 5×10^3 cells per 100 μL per well (n = 8 per group) and exposed for 24 h to mRNA-LNP at 0.1, 1, or 10 nM. Control groups included untreated cells, 5-fluorouracil (5-FU; 10 μM and 100 μM) as cytotoxic references, and 0.1% Triton X-100 as a positive control for complete cell lysis. Cell viability was measured using Cell Count Reagent SF (Nacalai Tesque, Inc., Kyoto, Japan; Cat# 07553-44) according to the manufacturer's instructions, and absorbance was recorded at 450 nm using a microplate reader.

For in vivo validation of hFAPCAR expression via mRNA-LNP delivery, splenocytes were collected from C57BL/6 mice 24 h after intravenous injection of hFAPCAR mRNA-LNP or PBS. For staining, FITC-anti-CD8β antibody (BioLegend, Cat.# 126605) and PE-labeled human FAP protein were premixed to prepare an antibody cocktail and added to the cell suspension (2×10^6 cells/100 μL). After incubation for 1 h at 4 °C, the cells were washed twice with PBS, followed by viability staining with 7-AAD (BioLegend, Cat.# 420403). FACS was performed on a BD FACSymphony S6, and data were analyzed using FlowJo v10.8.1. Gating was based on singlets, lymphocytes, and live cells. The PE-FMO (fluorescence-minus-one for the PE-hFAP channel) control was prepared from the control mouse and used to define the $hFAPCAR^+$ threshold.

Analysis of biodistribution in immunodeficient and immunocompetent tumor models

To visualize the biodistribution of FAPCAR-expressing splenocytes, a NanoLuc luciferase reporter system was employed. The NanoLuc luciferase mRNA was co-electroporated with FAPCAR mRNA into splenocytes, enabling bioluminescence imaging through the enzymatic oxidation of its substrate, furimazine. To ensure co-expression, the CAR construct was modified by replacing its intracellular signaling domain with NanoLuc luciferase, while retaining the extracellular antigen recognition domain, and an internal ribosome entry site (IRES) was inserted between the two coding sequences. Splenocytes were prepared and electroporated as described above, then intravenously injected into colorectal tumor-bearing mice, including both immunodeficient (NOD/SCID) and immunocompetent (C57BL/6) models. 24 hours after injection, the liver, kidney, and tumor tissues were harvested. A 0.6-mm biopsy sample was excised from each tissue and placed into 40 μL of PBS, followed by the addition of 40 μL of furimazine solution (1 μg/μL in dimethyl sulfoxide; Aobious, Gloucester, MA, USA; Cat.# AOB 36539). Luminescence intensity from each sample was measured using a microplate reader equipped for absorbance and fluorescence detection (SH-9000Lab, Corona Electric Co., Ltd., Ibaraki, Japan).

Efficacy testing in syngeneic models

For the syngeneic models, treatment was administered via intravenous tail injection on the next day following tumor cell inoculation for a total of four doses. Overall, the treatment regimen consisted of a chemotherapeutic agent (5-FU (10 mg/mL dissolved in PBS; 2 μL per injection; FUJIFILM Wako Pure Chemical Corp., Osaka, Japan; Cat.# 066-01402) for the MC38 models and the Renca models; CDDP (3 mg/mL dissolved in DMSO; 1 μL per injection; FUJIFILM Wako Pure Chemical Corp., Cat.# 039-20093) for the 4T1 models, E0771 models and the Renca models), immune checkpoint inhibitors (ICIs) (anti-mouse PD-1 (10 μL per injection; Bio X Cell, Lebanon, NH, USA; Cat# BE0273) and anti-mouse CTLA-4 (10 μL per injection; Bio X Cell, Cat# BE 0032)), and the mRNA-LNPs (10 μg mRNA). Each administration was adjusted to a total volume of 250 μL with PBS. Tumor volumes were estimated using the long (L) and short (W) diameters, with the formula $1/2 \times L \times W^2$.

Immunofluorescence staining of tumor tissue

Indirect immunofluorescence was performed on tumor tissues harvested from syngeneic MC38 tumor–bearing mice treated with mRNA-LNP, 5-FU, and ICIs. Briefly, after fixation, dehydration, and paraffin embedding, the tissues were sectioned at 6 μm, deparaffinized, and subjected to antigen retrieval. The sections were then incubated with mouse FAP protein tagged with a His tag, followed by secondary labeling with Alexa Fluor 594–conjugated anti-His antibody. Fluorescence signals were visualized using an all-in-one fluorescence microscope (BZ-X710; Keyence Corporation, Japan).

Rechallenge in the cured syngeneic models

As a rechallenge in the cured MC38 (colorectal) models, two mice that had achieved complete tumor regression following treatment with 5-FU, ICIs and mRNA-LNPs were rechallenged with both homologous and heterologous tumors. Specifically, MC38 + FAP-expressing cells were implanted subcutaneously into the dorsal region, while E0771 + FAP-expressing cells were implanted into the mammary fat pad. Subsequently, a second rechallenge with homologous tumors (MC38 + FAP-expressing cells) was performed in the mammary fat pad. Similarly, in the context of breast cancer, the three mice, previously treated and cured with a regimen of CDDP, ICIs and LNPs, were subjected to a rechallenge involving dorsal colorectal tumors (M38+FAP-expressing cells) and pectoral breast cancer tumors (4T1+FAP-expressing cells). The establishment and measurement of the tumors were consistent with the initial experiments. No treatment was conducted during the rechallenges.

Besides, three additional cured MC38 models were subjected to homologous tumor rechallenge under conditions of T cell depletion or sequestration. Starting one day prior to tumor cell implantation, mice received daily injections of either 160 μL of anti-CD8α antibody (1:16 dilution in PBS; intravenous; Bio X Cell, Cat# BE0004-1), 200 μL of Fingolimod hydrochloride (FTY720) (1:20 dilution from a 1 μg/μL DMSO stock; intraperitoneal; MedChemExpress, Monmouth Junction, NJ, USA; Cat# HY-12005), or 200 μL of PBS (intraperitoneal) as a control. On the following day, MC38 + FAP-expressing tumor cells were subcutaneously implanted into the dorsal region. To monitor $CD8^+$ T cell depletion, peripheral blood was collected from the submandibular vein and stained with fluorophore-conjugated anti-CD8β antibody, followed by FACS analysis. FlowJo 10.8.1 was used to analyze and visualize the data.

m^6A-modified mRNA synthesis and in vivo efficacy assessment

Therapeutic mRNA was synthesized as described above. For N6-methyladenosine (m^6A) modification, adenosine triphosphate (ATP) in the IVT reaction (Takara IVTpro™ T7 mRNA Synthesis System) was replaced with N6-methyladenosine-5′-triphosphate (TriLink, Cat# N-1013). The experiment was conducted in syngeneic colorectal tumor models. LNP formulation, establishment of tumor models, treatment regimen (including 5-FU and ICIs), and tumor volume measurement were performed as previously described.

Single cell RNA sequencing of relapsed and untreated tumor tissues

Tumor tissues were harvested from three syngeneic colorectal tumor models: two that had initially responded to treatment with 5-FU, ICIs, and LNPs but subsequently relapsed, and one that had not received any treatment. Approximately 10–15 mg of tissue per sample was minced in 2 mL of DMEM containing 10% FBS, ulinastatin (2 μg/mL), and sivelestat (2 μg/mL) on ice. Subsequently, 8 mL of digestion buffer (DMEM supplemented with Collagenase D and DNase) was added, and the mixture was incubated at 37 °C in a water bath with gentle shaking (100 rpm) for 1 hour. Following enzymatic digestion, the suspension was filtered through a 40 μm cell strainer, centrifuged at 380 × g for 5 minutes at 4 °C, and the pellet was resuspended in 1 mL of pre-warmed ACK lysis buffer (Thermo Fisher Scientific, Cat# A1049201) for 3 minutes at 37 °C. After red blood cell lysis,

9 mL of HBSS was added, followed by a second centrifugation step. The resulting cell pellet was resuspended in 0.05% BSA/PBS and adjusted to a final concentration of 1000 cells/μL in 50 μL for downstream single-cell RNA sequencing.

Single cell RNA sequencing (scRNA-seq) was performed using the 10x Genomics Chromium platform. The Gene Expression application was used to measure the expression levels of transcripts across the entire genome for each cell. The sequencing data was processed using the Cell Ranger pipeline (10x Genomics, cellranger 7.1.0) for initial demultiplexing, alignment to the reference genome, and generation of feature-barcode matrices. These steps were conducted by the Osaka University Bioinformatics Center.

Cell Ranger output files were imported into Seurat (v4.4.0) under R (v4.2.2) for preprocessing. Quality control was conducted by filtering cells with mitochondrial gene percentage ≥ 15%, fewer than 500 or more than 3000 detected genes, or genes detected in fewer than three cells, followed by doublet removal with scDblFinder (v1.12.0). Gene expression counts were normalized with SCTransform (v0.4.1), and 3000 highly variable features were selected for integration. Data integration across samples was performed with FindIntegrationAnchors and IntegrateData functions, followed by dimensionality reduction with PCA and batch correction using Harmony (v1.2.3). The top 16 Harmony dimensions were used for neighbor graph construction, clustering (resolution = 0.5), and UMAP visualization. Differentially expressed marker genes for each cluster were identified using FindAllMarkers with thresholds of min.pct = 0.25 and logfc.threshold = 0.25. The top 10 markers per cluster were exported for annotation, and clusters were manually annotated based on canonical cell type markers. Expression patterns of tissue-resident memory T cell (Trm) markers (Cd3d, Cd8a, Cd69, Itgae) were visualized using DotPlot, and expression patterns of Cd74 and Mif were visualized with FeaturePlot.

Cell–cell communication analysis was performed using CellChat (v1.6.1). The CellChat mouse database (CellChatDB.mouse) was subset to include "Secreted Signaling", "ECM-Receptor", and "Cell-Cell Contact" pathways. Overexpressed genes and interactions were identified, and communication probabilities were computed with a minimum cell threshold of 10. Pathway-level communication probabilities were aggregated for centrality analysis, and outgoing and incoming signaling roles were visualized as heatmaps.

MIF-CD74 blockade in syngeneic colorectal tumor models

To assess the functional contribution of the MIF-CD74 axis, neutralizing antibodies were administered intravenously in combination with m^6A-modified mRNA-LNPs, 5-FU, and ICIs in syngeneic colorectal tumor models. Specifically, rabbit anti-CD74 (Abcam, Cambridge, UK; Cat# ab289891; 5 μg per 25 g body weight) and goat anti-MIF (Bio-Techne, Minneapolis, MN, USA; Cat# AF-289-PB; 5 μg per 25 g) were used. All other procedures, including tumor model establishment, treatment regimen, and tumor volume measurements, followed previously described protocols.

Efficacy testing in patient-derived xenograft (PDX) models

For the PDX models, treatment was administered via intravenous injection every other day for a total of two doses. Each injection contained 3*10^7 splenocytes pre-incubated with 10 μg mRNA-LNPs, and the total injection volume was adjusted to 250 μL with PBS. Splenocytes were isolated from the spleens of immunocompetent C57BL/6 background mice using the method described above and cultured in DMEM supplemented with 10% FBS and 100 ng/mL IL-2. The mRNA-LNPs were added to the culture medium and incubated with the splenocytes for 30 minutes at 37°C in 5% CO_2 prior to injection. For the PDX-1 models, one mouse was treated with splenocytes derived from a 7SL1 knock-in mouse, while another one received an equal volume of PBS as a control. For the PDX-2 models, two mice received splenocytes from a wild-type (WT) mouse and a 7SL1 knock-in mouse, respectively, while the third mouse was administered PBS as a control. mRNA-LNPs (containing non-m^6A-modified mRNA) and tumor volume measurements were performed according to previously described protocols.

RNA sequencing (RNA-seq) and assay for transposase-accessible chromatin using sequencing (ATAC-seq) of PDX tumor tissues

For bulk RNA-seq, tumor tissues were cut into 6 mm pieces, immersed in RNA later solution (Thermo Fisher Scientific, Cat.# AM7020), and stored at -150 °C for cryopreservation. Total RNA from the tissues was isolated using ISOGEN (Nippon Gene Co., Ltd., Cat.# 311-02501) according to the manufacturer's instruction, after which the concentration and the quality were assessed by NanoDrop. The purified RNA was sent to the Microbiology Research Institute for RNA-seq. Ribosomal RNA was depleted using the Ribo-Zero Plus rRNA Depletion Kit (Illumina, San Diego, CA, USA), and mRNA was prepared using the TruSeq Stranded mRNA Sample Preparation Kit (Illumina) without the mRNA Purification Beads (RPB) step. Sequencing was performed using the NovaSeq6000 platform in 101 bp x 101 bp paired-end mode. Read mapping and gene expression quantification were performed using the Rhelixa RNA-seq pipeline (Rhelixa Inc., Tokyo, Japan) on the supercomputer system at the National Institute of Genetics (NIG), Japan. Sequence quality of the FASTQ files was assessed using FastQC, and reads were trimmed based on quality scores using Trimmomatic. Trimmed reads were aligned to the human reference genome (hg19) using Hisat2. The resulting SAM files were converted to BAM format with Samtools, and gene-level read counts (Supplementary Data S1) were generated using featureCounts. Differential gene expression analysis was performed using DESeq2, and pathway enrichment analysis was conducted using clusterProfiler. Transcription factor identification was performed using ChIP-X Enrichment Analysis 3 (ChEA3) based on the top differentially expressed genes (DEGs).

For ATAC-seq, approximately 20-30 mg of tumor tissue was immediately snap-frozen and stored at -150 °C until library preparation. ATAC-seq libraries were prepared using the ATAC-Seq Kit (Active Motif, Inc., Carlsbad, CA, USA; Cat.# 53150) according to the manufacturer's protocol. The tagmentation reaction and DNA purification were performed in-house, while the subsequent PCR amplification of the tagmented DNA

and sequencing were carried out at the Microbiology Research Institute. Sequencing was performed on the NovaSeq 6000 platform in 151 bp x 151 bp paired-end mode. Read mapping and gene expression quantification were performed using the Rhelixa RNA-seq pipeline (Rhelixa Inc.) on the supercomputer system at the National Institute of Genetics (NIG), Japan. Sequence quality of the FASTQ files was assessed using FastQC, and reads were trimmed based on quality scores using Trimmomatic. Trimmed reads were aligned to the human reference genome (hg19) using Hisat2. The resulting SAM files were converted to BAM format with Samtools, Peak calling (Data S2-S4) was performed using Model-based Analysis of ChIP-seq 2 (MACS2) with the sorted BAM files. The resulting narrowPeak files were used for peak annotation and classification using the ChIPseeker package in R. Visualization of mapped reads was carried out using Integrative Genomics Viewer (IGV), with the sorted BAM files as input.

Statistical analysis

The details of each experiment are provided in the figure legends. All statistical analyses were performed using GraphPad Prism 10.1.1. For comparisons among multiple groups, one-way or two-way analysis of variance (ANOVA) with post hoc Tukey's or Bonferroni's test was employed, depending on the experimental setup. Kaplan-Meier survival curves were analyzed using the log-rank test.

For each experiment, the number of replicates (n) and the specific statistical test performed are detailed in the corresponding figure legends. A P-value of <0.05 was considered statistically significant. All analyses were conducted in accordance with standard statistical practices to ensure reproducibility and reliability.

Data availability

The integrated output file of scRNA-seq data in Fig. 2d-f and Fig. S2i, as well as the results of CellChat analysis, are available as R-readable .rds files on Zenodo (https://zenodo.org/records/16756958). The count data from RNA-seq on PDX are provided as Supplementary Data S1, and the peak files generated by MACS2 from ATAC-seq as Supplementary Data S2-4. The ATAC-seq, RNA-seq and scRNA-seq data have been deposited in NCBI's Gene Expression Omnibus (Edgar et al., 2002) and are accessible through GEO Series accession number GSE307697 (https://www.ncbi.nlm.nih.gov/geo/query/acc.cgi?acc=GSE307697), GSE307698 (https://www.ncbi.nlm.nih.gov/geo/query/acc.cgi?acc=GSE307698) and GSE307699 (https://www.ncbi.nlm.nih.gov/geo/query/acc.cgi?acc=GSE307699).

Received: 30 August 2025; Accepted: 29 November 2025
Published online: 10 December 2025

References

1. Yamaguchi, H. & Miyazaki, M. Heterocellular adhesion in cancer invasion and metastasis: interactions between cancer cells and cancer-associated fibroblasts. *Cancers (Basel)* https://doi.org/10.3390/cancers16091636 (2024).
2. Arner, E. N. & Rathmell, J. C. Metabolic programming and immune suppression in the tumor microenvironment. *Cancer Cell* **41**, 421–433. https://doi.org/10.1016/j.ccell.2023.01.009 (2023).
3. Giraudo, M. F., Jackson, Z., Das, I., Abiona, O. M. & Wald, D. N. Chimeric antigen receptor (CAR)-T cell therapy for non-hodgkin's lymphoma. *Pathog. Immun.* **9**, 1–17. https://doi.org/10.20411/pai.v9i1.647 (2024).
4. Pereira, R. & Bergantim, R. An assessment of the effectiveness and safety of chimeric antigen receptor T-cell therapy in multiple myeloma patients with relapsed or refractory disease: a systematic review and meta-analysis. *Int. J. Mol. Sci.* https://doi.org/10.3390/ijms25094996 (2024).
5. Patel, K. K., Tariveranmoshabad, M., Kadu, S., Shobaki, N. & June, C. From concept to cure: the evolution of CAR-T cell therapy. *Mol. Ther.* **33**, 2123–2140. https://doi.org/10.1016/j.ymthe.2025.03.005 (2025).
6. Albelda, S. M. CAR T cell therapy for patients with solid tumours: key lessons to learn and unlearn. *Nat. Rev. Clin. Oncol.* **21**, 47–66. https://doi.org/10.1038/s41571-023-00832-4 (2024).
7. Adams, S. C. et al. Immunotherapies for locally aggressive cancers. *Adv. Drug Deliv. Rev.* **210**, 115331. https://doi.org/10.1016/j.addr.2024.115331 (2024).
8. Xiao, Y. & Yu, D. Tumor microenvironment as a therapeutic target in cancer. *Pharmacol. Ther.* **221**, 107753. https://doi.org/10.1016/j.pharmthera.2020.107753 (2021).
9. Ceelen, W., Ramsay, R. G., Narasimhan, V., Heriot, A. G. & De Wever, O. Targeting the tumor microenvironment in colorectal peritoneal metastases. *Trends Cancer* **6**, 236–246. https://doi.org/10.1016/j.trecan.2019.12.008 (2020).
10. Chen, Y. et al. Comprehensive molecular classification predicted microenvironment profiles and therapy response for HCC. *Hepatology* **80**, 536–551. https://doi.org/10.1097/hep.0000000000000869 (2024).
11. Jenkins, L. et al. Cancer-associated fibroblasts suppress CD8+ T-cell infiltration and confer resistance to immune-checkpoint blockade. *Cancer Res.* **82**, 2904–2917. https://doi.org/10.1158/0008-5472.Can-21-4141 (2022).
12. Yang, D., Liu, J., Qian, H. & Zhuang, Q. Cancer-associated fibroblasts: from basic science to anticancer therapy. *Exp. Mol. Med.* **55**, 1322–1332. https://doi.org/10.1038/s12276-023-01013-0 (2023).
13. Wan, P. K., Ryan, A. J. & Seymour, L. W. Beyond cancer cells: Targeting the tumor microenvironment with gene therapy and armed oncolytic virus. *Mol. Ther.* **29**, 1668–1682. https://doi.org/10.1016/j.ymthe.2021.04.015 (2021).
14. Zhang, H. et al. Define cancer-associated fibroblasts (CAFs) in the tumor microenvironment: new opportunities in cancer immunotherapy and advances in clinical trials. *Mol. Cancer* **22**, 159. https://doi.org/10.1186/s12943-023-01860-5 (2023).
15. Hartmann, K. P. et al. FAP-retargeted Ad5 enables in vivo gene delivery to stromal cells in the tumor microenvironment. *Mol. Ther.* **31**, 2914–2928. https://doi.org/10.1016/j.ymthe.2023.08.018 (2023).
16. Halbrook, C. J., Lyssiotis, C. A., Pasca di Magliano, M. & Maitra, A. Pancreatic cancer: advances and challenges. *Cell* **186**, 1729–1754. https://doi.org/10.1016/j.cell.2023.02.014 (2023).
17. Argentiero, A. et al. The complexity of the tumor microenvironment in hepatocellular carcinoma and emerging therapeutic developments. *J. Clin. Med.* https://doi.org/10.3390/jcm12237469 (2023).
18. Lekan, A. A. & Weiner, L. M. The role of chemokines in orchestrating the immune response to pancreatic ductal adenocarcinoma. *Cancers (Basel)* https://doi.org/10.3390/cancers16030559 (2024).
19. Xiao, Z. et al. Desmoplastic stroma restricts T cell extravasation and mediates immune exclusion and immunosuppression in solid tumors. *Nat. Commun.* **14**, 5110. https://doi.org/10.1038/s41467-023-40850-5 (2023).
20. Chhabra, Y. & Weeraratna, A. T. Fibroblasts in cancer: unity in heterogeneity. *Cell* **186**, 1580–1609. https://doi.org/10.1016/j.cell.2023.03.016 (2023).

21. Bruni, D., Angell, H. K. & Galon, J. The immune contexture and Immunoscore in cancer prognosis and therapeutic efficacy. *Nat. Rev. Cancer* **20**, 662–680. https://doi.org/10.1038/s41568-020-0285-7 (2020).
22. Shahvali, S., Rahiman, N., Jaafari, M. R. & Arabi, L. Targeting fibroblast activation protein (FAP): advances in CAR-T cell, antibody, and vaccine in cancer immunotherapy. *Drug Deliv. Transl. Res.* **13**, 2041–2056. https://doi.org/10.1007/s13346-023-01308-9 (2023).
23. Li, H. et al. FAP-targeted delivery of radioiodinated probes: a progressive albumin-driven strategy for tumor theranostics. *J. Control Release* **382**, 113678. https://doi.org/10.1016/j.jconrel.2025.113678 (2025).
24. Zhang, Z. et al. From basic research to clinical application: targeting fibroblast activation protein for cancer diagnosis and treatment. *Cell Oncol. (Dordr)* **47**, 361–381. https://doi.org/10.1007/s13402-023-00872-z (2024).
25. Bocci, M. et al. In vivo activation of FAP-cleavable small molecule-drug conjugates for the targeted delivery of camptothecins and tubulin poisons to the tumor microenvironment. *J. Control Release* **367**, 779–790. https://doi.org/10.1016/j.jconrel.2024.02.014 (2024).
26. Yamazaki, M. & Ishimoto, T. Targeting cancer-associated fibroblasts: eliminate or reprogram?. *Cancer Sci.* **116**, 613–621. https://doi.org/10.1111/cas.16443 (2025).
27. Meng, S., Hara, T., Miura, Y. & Ishii, H. Fibroblast activation protein constitutes a novel target of chimeric antigen receptor T-cell therapy in solid tumors. *Cancer Sci.* **115**, 3532–3542. https://doi.org/10.1111/cas.16285 (2024).
28. Sato, Y., Nakamura, T., Yamada, Y. & Harashima, H. The impact of, and expectations for, lipid nanoparticle technology: from cellular targeting to organelle targeting. *J. Control Release* **370**, 516–527. https://doi.org/10.1016/j.jconrel.2024.05.006 (2024).
29. Parhiz, H., Atochina-Vasserman, E. N. & Weissman, D. mRNA-based therapeutics: looking beyond COVID-19 vaccines. *Lancet* **403**, 1192–1204. https://doi.org/10.1016/s0140-6736(23)02444-3 (2024).
30. Unruh, T. et al. Mesoscopic structure of lipid nanoparticle formulations for mRNA drug delivery: comirnaty and drug-free dispersions. *ACS Nano.* **18**, 9746–9764. https://doi.org/10.1021/acsnano.4c02610 (2024).
31. Nie, S., Qin, Y., Ou, L., Chen, X. & Li, L. In Situ reprogramming of immune cells using synthetic nanomaterials. *Adv. Mater.* **36**, e2310168. https://doi.org/10.1002/adma.202310168 (2024).
32. Meng, S. et al. In Vivo Engineered CAR-T Cell Therapy: Lessons Built from COVID-19 mRNA Vaccines. *Int. J. Mol. Sci.* https://doi.org/10.3390/ijms26073119 (2025).
33. Rurik, J. G. et al. CAR T cells produced in vivo to treat cardiac injury. *Science* **375**, 91–96. https://doi.org/10.1126/science.abm0594 (2022).
34. Álvarez-Benedicto, E. et al. Spleen SORT LNP generated in situ CAR T cells extend survival in a mouse model of lymphoreplete B cell lymphoma. *Angew. Chem. Int. Ed. Engl.* **62**, e202310395. https://doi.org/10.1002/anie.202310395 (2023).
35. Billingsley, M. M. et al. In Vivo mRNA CAR T cell engineering via targeted ionizable lipid nanoparticles with extrahepatic tropism. *Small* **20**, e2304378. https://doi.org/10.1002/smll.202304378 (2024).
36. Michels, A., Ho, N. & Buchholz, C. J. Precision medicine: In vivo CAR therapy as a showcase for receptor-targeted vector platforms. *Mol. Ther.* **30**, 2401–2415. https://doi.org/10.1016/j.ymthe.2022.05.018 (2022).
37. Chijimatsu, R. et al. Establishment of a reference single-cell RNA sequencing dataset for human pancreatic adenocarcinoma. *Science* **25**, 104659. https://doi.org/10.1016/j.isci.2022.104659 (2022).
38. Mu, S., Zhao, K., Zhong, S. & Wang, Y. The Role of m6A Methylation in Tumor Immunity and Immune-Associated Disorder. *Biomolecules* https://doi.org/10.3390/biom14081042 (2024).
39. Hara, T. et al. High N6-methyladenosine-activated TCEAL8 mRNA is a novel pancreatic cancer marker. *Cancer Sci.* **115**, 2360–2370. https://doi.org/10.1111/cas.16152 (2024).
40. Strijker, J. G. M. et al. Blocking MIF secretion enhances CAR T-cell efficacy against neuroblastoma. *Eur. J. Cancer* **218**, 115263. https://doi.org/10.1016/j.ejca.2025.115263 (2025).
41. Johnson, L. R. et al. The immunostimulatory RNA RN7SL1 enables CAR-T cells to enhance autonomous and endogenous immune function. *Cell* **184**, 4981-4995.e4914. https://doi.org/10.1016/j.cell.2021.08.004 (2021).
42. Zhou, Z., Xia, Y., Chen, R., Gao, P. & Duan, S. Unveiling a novel fusion gene enhances CAR T cell therapy for solid tumors. *Mol. Cancer* **23**, 98. https://doi.org/10.1186/s12943-024-02007-w (2024).
43. Nishimura, C. D. et al. TOP CAR with TMIGD2 as a safe and effective costimulatory domain in CAR cells treating human solid tumors. *Sci. Adv.* **10**, eadk1857. https://doi.org/10.1126/sciadv.adk1857 (2024).
44. Leland, P. et al. Identification and characterisation of novel CAR-T cells to target IL13Rα2 positive human glioma in vitro and in vivo. *Clin. Transl. Med.* **14**, e1664. https://doi.org/10.1002/ctm2.1664 (2024).
45. Amorós-Pérez, B., Rivas-Pardo, B., Gómez, M., Del Moral, J. L. & Martínez-Naves, S. E. State of the art in car-t cell therapy for solid tumors: is there a sweeter future?. *Cells* https://doi.org/10.3390/cells13090725 (2024).
46. Rojas-Quintero, J. et al. Car T cells in solid tumors: overcoming obstacles. *Int. J. Mol. Sci.* https://doi.org/10.3390/ijms25084170 (2024).
47. Cappell, K. M. & Kochenderfer, J. N. Long-term outcomes following CAR T cell therapy: what we know so far. *Nat. Rev. Clin. Oncol.* **20**, 359–371. https://doi.org/10.1038/s41571-023-00754-1 (2023).
48. Bimbo, J. F. et al. T cell-specific non-viral DNA delivery and in vivo CAR-T generation using targeted lipid nanoparticles. *J Immunother Cancer* https://doi.org/10.1136/jitc-2025-011759 (2025).
49. Park, J. et al. Alliance with EPR effect: combined strategies to improve the EPR effect in the tumor microenvironment. *Theranostics* **9**, 8073–8090. https://doi.org/10.7150/thno.37198 (2019).
50. Belyaev, I. B., Griaznova, O. Y., Yaremenko, A. V., Deyev, S. M. & Zelepukin, I. V. Beyond the EPR effect: Intravital microscopy analysis of nanoparticle drug delivery to tumors. *Adv. Drug Deliv. Rev.* **219**, 115550. https://doi.org/10.1016/j.addr.2025.115550 (2025).
51. Plaks, V. et al. CD19 target evasion as a mechanism of relapse in large B-cell lymphoma treated with axicabtagene ciloleucel. *Blood* **138**, 1081–1085. https://doi.org/10.1182/blood.2021010930 (2021).
52. Zhang, M. et al. Advances in cancer immunotherapy: historical perspectives, current developments, and future directions. *Mol Cancer* **24**, 136. https://doi.org/10.1186/s12943-025-02305-x (2025).
53. Reena, R. D. S. et al. Overcoming tumor antigen heterogeneity in CAR-T cell therapy for malignant mesothelioma (MM). *J. Cancer Metastasis Treat.* **8**, 28. https://doi.org/10.20517/2394-4722.2022.51 (2022).
54. Du, B. et al. CAR-T therapy in solid tumors. *Cancer Cell* **43**, 665–679. https://doi.org/10.1016/j.ccell.2025.03.019 (2025).
55. Christo, S. N., Park, S. L., Mueller, S. N. & Mackay, L. K. The multifaceted role of tissue-resident memory T cells. *Annu. Rev. Immunol.* **42**, 317–345. https://doi.org/10.1146/annurev-immunol-101320-020220 (2024).
56. Schenkel, J. M. & Pauken, K. E. Localization, tissue biology and T cell state - implications for cancer immunotherapy. *Nat. Rev. Immunol.* **23**, 807–823. https://doi.org/10.1038/s41577-023-00884-8 (2023).
57. Virassamy, B. et al. Intratumoral CD8(+) T cells with a tissue-resident memory phenotype mediate local immunity and immune checkpoint responses in breast cancer. *Cancer Cell* **41**, 585-601.e588. https://doi.org/10.1016/j.ccell.2023.01.004 (2023).
58. Zaccara, S. & Jaffrey, S. R. A unified model for the function of YTHDF proteins in regulating m(6)A-modified mRNA. *Cell* **181**, 1582-1595.e1518. https://doi.org/10.1016/j.cell.2020.05.012 (2020).
59. Lu, X. et al. HIF-1α-induced expression of the m6A reader YTHDF1 inhibits the ferroptosis of nucleus pulposus cells by promoting SLC7A11 translation. *Aging Cell* **23**, e14210. https://doi.org/10.1111/acel.14210 (2024).
60. Li, Y., Xiao, Z., Wang, Y., Zhang, D. & Chen, Z. The m6A reader IGF2BP2 promotes esophageal cell carcinoma progression by enhancing EIF4A1 translation. *Cancer Cell Int.* **24**, 162. https://doi.org/10.1186/s12935-024-03349-7 (2024).

61. Han, J. et al. Novel insights into the links between n6-methyladenosine and regulated cell death in musculoskeletal diseases. *Biomolecules* https://doi.org/10.3390/biom14050514 (2024).
62. Shah, N. & Sukumar, S. The Hox genes and their roles in oncogenesis. *Nat. Rev. Cancer* **10**, 361–371. https://doi.org/10.1038/nrc2826 (2010).
63. Calvo, R. *et al.* Altered HOX and WNT7A expression in human lung cancer. *Proc Natl Acad Sci U S A* **97** 12776-12781 https://doi.org/10.1073/pnas.97.23.12776 (2000)
64. Shen, W. F. et al. HOXA9 forms triple complexes with PBX2 and MEIS1 in myeloid cells. *Mol. Cell Biol.* **19**, 3051–3061. https://doi.org/10.1128/mcb.19.4.3051 (1999).
65. Guerra, S. L. et al. A deregulated HOX gene axis confers an epigenetic vulnerability in KRAS-mutant lung cancers. *Cancer Cell* **37**, 705-719.e706. https://doi.org/10.1016/j.ccell.2020.03.004 (2020).
66. Zinzi, A. et al. Late relapse after CAR-T cell therapy for adult patients with hematologic malignancies: A definite evidence from systematic review and meta-analysis on individual data. *Pharmacol. Res.* **190**, 106742. https://doi.org/10.1016/j.phrs.2023.106742 (2023).

Acknowledgement

Acknowledgement The authors thank all laboratory members for their valuable support and discussions. We acknowledge the Research Institute for Microbial Diseases, the University of Osaka, for assistance with RNA-seq, ATAC-seq and scRNA-seq. RNA-seq data analysis was conducted using the Rhelixa RNAseq pipeline provided by Rhelixa, Inc. Computational analyses were partially carried out on the NIG supercomputer at the ROIS National Institute of Genetics. The schemata were created using BioRender.

Author contributions

S.M., T.Ha., H.E., and H.I conceptualized the study and the objectives, and S.M., T.Ha., T.Hi., S.R., Ta.S., K.O., Y.M., M.M., Y.D., H.E., and H.I designed the experiment. S.M., T.Ha., Te.S., S.T., Y.A., Y.S., D.M., Y.M., and H.I. performed the experiments and acquired the data. S.M., T.Ha., Te.S., S.T., and H.I. contributed to the data analysis. S.M., T.Ha. and H.I gave input in the manuscript and figures. All authors have read and approved the final manuscript version for publication.

Funding

This work was supported in part by a Grant-in-Aid for Scientific Research from the Ministry of Education, Culture, Sports, Science and Technology (23K18313, 24K02518, 23KK0153, 24K22144, 23K19505, 24K19992, 25H01060) and by AMED under Grant Number JP23ym0126809, JP24ym0126809. Partial support was offered by the Institute for Fermentation, Osaka (G2024-3-006) to H.I, and Suzuken Memorial Foundation, Kobayashi Foundation, Grant of The Clinical Research Promotion Foundation and The Uehara Memorial Foundation to S.M.

Declarations

Competing interests

Partial institutional endowments were received from Hirotsu Bio Science Inc. (Tokyo, Japan), Kinshu-kai Medical Corporation (Osaka, Japan), Kyowa-kai Medical Corporation (Kawanishi, Hyogo and Osaka, Japan), IDEA Consultants Inc. (Tokyo, Japan), and Unitech Co. Ltd. (Chiba, Japan).

Ethics

All animals in this study were cared according to Osaka University's standards for care and use of laboratory animals, and operation procedures were performed in accordance with protocols approved by the Laboratory Investigation Committee, Osaka University Medical School (Approval No. 04-105-014).
All patient-derived tumor tissues used for PDX establishment were purchased from the Central Institute for Experimental Medicine and Life Science. The institute confirmed that all human samples were collected with informed consent from donors and with approval from the appropriate institutional ethics committee, in compliance with all relevant guidelines and regulations. No human participants were directly involved in this study.

Additional information

Supplementary Information The online version contains supplementary material available at https://doi.org/10.1038/s41598-025-31128-5.

Correspondence and requests for materials should be addressed to H.I.

Reprints and permissions information is available at www.nature.com/reprints.

Publisher's note Springer Nature remains neutral with regard to jurisdictional claims in published maps and institutional affiliations.

Open Access This article is licensed under a Creative Commons Attribution-NonCommercial-NoDerivatives 4.0 International License, which permits any non-commercial use, sharing, distribution and reproduction in any medium or format, as long as you give appropriate credit to the original author(s) and the source, provide a link to the Creative Commons licence, and indicate if you modified the licensed material. You do not have permission under this licence to share adapted material derived from this article or parts of it. The images or other third party material in this article are included in the article's Creative Commons licence, unless indicated otherwise in a credit line to the material. If material is not included in the article's Creative Commons licence and your intended use is not permitted by statutory regulation or exceeds the permitted use, you will need to obtain permission directly from the copyright holder. To view a copy of this licence, visit http://creativecommons.org/licenses/by-nc-nd/4.0/.

© The Author(s) 2025